A 16-Channel Dual-Row Transmit Array in Combination with a 31-Element Receive Array for Human Brain Imaging at 9.4 T

G. Shajan,[1]* Mikhail Kozlov,[2] Jens Hoffmann,[1] Robert Turner,[2] Klaus Scheffler,[1,3] and Rolf Pohmann[1]

Purpose: Arranging transmit array elements in multiple rows provides an additional degree of freedom to correct B_1^+ field inhomogeneities and to achieve whole-brain excitation at ultra-high field strengths. Receive arrays shaped to the contours of the anatomy increase the signal-to-noise ratio of the image. In this work, the advantages offered by the transmit and receive array techniques are combined for human brain imaging at 9.4 T.

Methods: A 16-element dual-row transmit array and a 31-element receive array were developed. Based on an accurate numerical model of the transmit array, the deposited power was calculated for different head sizes and positions. The influence of the receive array on the transmit field was characterized. Parallel imaging performance and signal-to-noise ratio of the receive array were evaluated.

Results: On average, a two fold increase in signal-to-noise ratio was observed in the whole-brain volume when compared with a 16-channel elliptic microstrip transceiver array. The benefits of combining the two arrays, B_1^+ shimming in three directions and high receive sensitivity, are demonstrated with high-resolution in vivo images.

Conclusion: The dual-row transmit array provides whole-brain coverage at 9.4 T, which, in combination with the helmet-shaped receive array, is a valuable radio frequency configuration for ultra-high field magnetic resonance imaging of the human brain. **Magn Reson Med 71:870–879, 2014. © 2013 Wiley Periodicals, Inc.**

Key words: transmit array; receive array; 9.4 T

INTRODUCTION

Remarkable progress has been made in addressing radio frequency (RF)-related challenges in magnetic resonance imaging (MRI) at ultra-high field (UHF) (1–3). An array of transmit elements is an essential tool to mitigate transmit field (B_1^+) inhomogeneities caused by the shorter wavelength in tissue, because it offers the flexibility to independently influence the amplitude and phase of the current in the individual coil elements. A variety of transceiver array designs, with coil elements arranged in single row or multiple rows, has been proposed for human brain imaging at 7 T and above (4–10).

The B_1^+ inhomogeneities caused by constructive and destructive interferences are even more severe at 9.4 T than at 7 T, which makes it difficult to achieve whole-brain coverage due to the field dropouts seen in the lower temporal lobes and cerebellum in the circularly polarized (CP) mode, even with relatively long coil elements (4). To improve longitudinal coverage and the RF shim capability in the z-direction, several research groups have already reported experimental (6–10) as well as numerical results (11,12) on the use of coil elements arranged in multiple rows. There is no significant difference in the transmit field pattern of a single-row array when compared with multiple-row transmit arrays if they are of similar length and driven in CP mode. However, multiple rows of transmit elements provide additional degrees of freedom to manipulate the transmit field using RF shimming methods for improved coverage of the lower brain (6–13). Special attention has to be paid to the power deposited in the tissue at 400 MHz, because this power loss can be highly localized and is not uniform over the entire volume (14). Therefore, realistic numerical simulations are essential to understand the RF field behavior in the MR environment in order to estimate the power deposited in the tissue and the local specific absorption rate (SAR).

The number of channels in most transceiver arrays presented up to now range from 8 to 16, depending on the available RF hardware in the scanner. Covering the same brain volume with a higher number of smaller receive elements on close-fitting, shaped helmets (15–18) results in significant signal-to-noise ratio (SNR) gain close to the array without losing sensitivity at larger distances (19) and improves parallel imaging performance due to the larger number of independent receive elements that are distributed in all spatial directions (20–22). The latter is an important factor in realizing the advantages of UHF MRI, as the reduced wavelength at high resonance frequency results in more distinct coil sensitivities and hence more effective sensitivity encoding (23).

In this work, we aim to evaluate the benefits offered by transmission and reception techniques using

[1]High-Field MR Center, Max Planck Institute for Biological Cybernetics, Tübingen, Germany.

[2]Department of Neurophysics, Max Planck Institute for Human Cognitive and Brain Sciences, Leipzig, Germany.

[3]Department of Biomedical Magnetic Resonance, University of Tübingen, Tübingen, Germany.

*Correspondence to: G. Shajan, M.E., High-Field MR Center, Max Planck Institute for Biological Cybernetics, Spemannstr. 41, 72076 Tübingen, Germany, E-mail: shajan.gunamony@tuebingen.mpg.de

individual arrays in MRI at 9.4 T. Thirty-one receive elements (to maintain symmetry, as described later) were arranged on a close-fitting helmet, and the receive array was combined with a 16-channel dual-row transmit array. The transmit performance and peak SAR averaged over 10 g of tissue (SAR_{10g}) were characterized in the CP mode. RF shimming was applied to improve transmit field homogeneity for high-quality, high-resolution whole-brain images in human subjects.

METHODS

The coil arrays were tested on a 9.4-T whole-body scanner (Siemens Healthcare, Erlangen, Germany), fitted with a head gradient insert (AC84; Siemens Healthcare) and equipped with 32 receive channels and a 7.5-kW RF amplifier (Advanced Energy Industries Inc., Fort Collins, CO, USA). To feed the 16 transmit elements, the RF signal was split into 16 components with equal amplitude and phase using a 1×16 power splitter (Werlatone, Brewster, NY, USA). RF shimming was restricted to static phase shimming, in which the transmit phase was adjusted by varying the length of the coaxial cable between the power splitter and the coil input. For CP mode excitation, the relative phase increment between neighboring elements was 22.5°.

Bench measurements were performed using a calibrated network analyzer (4396B; Agilent Technologies Inc., CA, USA) together with an 85046A *S*-parameter test set. The noise figure of the transmit/receive (TR) switch with preamplifier was measured using an Agilent N8973A noise figure meter and N4000A noise source. We imaged healthy volunteers who had signed a written consent form approved by the institutional review board of the University of Tübingen.

Transmit Array Construction

The transmit coil was constructed on a 2.5 mm thick fiber glass tube with an inner diameter of 28 cm. It consists of 16 identical rectangular loops (85 mm × 100 mm) arranged in two rows of eight elements each. A 12-mm gap was provided between the elements of the same row and between the rows. Lower row elements were rotated by 22.5° with respect to the upper row. All adjacent elements were inductively decoupled (24). Pads for soldering components were etched on a single-sided polyimide laminate (Novaclad® Laminate, Sheldahl, MN, USA) and attached to the fiber glass tube. A total of 13 fixed capacitors (5.6 pF, C-series; American Technical Ceramics, NY, USA, and Dalian Dalicap Co., Ltd., China) and one variable capacitor (5610; Johanson Manufacturing Corporation, NJ, USA) were distributed with equal spacing in each loop made of 2-mm-diameter silver wire. To actively detune the coil elements, a PIN diode (MA4PK2000, MA, USA) in series with an inductor was connected in parallel to one of the capacitors in each loop. This configuration requires sufficient reverse bias across the PIN diode to hold it in high-impedance state during spin excitation. The self-generated reverse bias direct current (DC) voltage that allowed the diode to operate in reverse-bias condition was measured as explained in Ref. 25. Furthermore, a measurement of flip angle versus transmit voltage (26) showed linear behavior up to the maximum power that can be applied per transmit coil element.

Miniaturized versions (30 mm × 60 mm) of previously presented TR switches (4) with preamplifiers were included inside the coil housing. Even though this coil was not optimized for receive performance, adding receive capability provided two main benefits: first, it can be combined with non-proton coils where proton images are needed for localization, although additional cable traps might be required at the X-nuclei frequency; and second, the external TR switch modules that are used in most transceiver arrays (3,4) are removed, which simplifies the setup and reduces the loss in the receive path.

Cables with equal phase length were connected between the TR switch and each element input. The cables to the second-row elements were routed in such a way that there was minimal influence on the reflection and transmission parameters of the two adjacent elements in the first row. The DC signal to actively detune the second-row elements was inserted into the RF cable through a bias tee. DC wiring and RF cabling were limited by the lack of space around the coil inside the head gradient. Great care was taken to complete the wiring without affecting the characteristics of the individual coil elements. The transmit ports of the 16-TR switches were connected to two customized eight-channel non-magnetic high-power modular connectors (ODU Steckverbindungssysteme GmbH & Co. KG, Mühldorf, Germany). A picture of the completed coil assembly is shown in Figure 1a, with the element numbering presented in Figure 1b.

Receive Array Construction

A tight-fitting helmet (left/right: 185 mm; anterior/posterior (AP): 220 mm; head/foot: 200 mm) with 3 mm wall thickness was fabricated by a three-dimensional (3D) printer (Eden 250; Objet GmbH, Germany). A total of 31 receive elements were arranged in four rows covering a length of 180 mm along the *z*-direction (Fig. 2a). In each of the first two rows, 10 elements formed two complete rings around the helmet. The third and fourth rows consisted of symmetrically arranged partial rings with seven and four elements, respectively. The layout and dimensions of the receive array elements are shown in Figure 2a. A combination of inductive decoupling and geometric overlap (27) was adopted to cancel the inductive coupling between neighboring coil elements. A 10-mm gap (8 mm for row 1) was maintained between the adjacent elements in the same row, and the coupling between these elements was minimized by inductive decoupling, which leads to smaller element size and larger separation between the non-neighboring coil elements. Each lower row element geometrically overlaps with two from the upper row. The elements in the first row were tapered to cover the helmet's dome. As adding an additional element to the third or fourth row would spoil the left–right symmetry, the 32nd receive channel was not used (Fig. 2a).

To tune the coil elements to the Larmor frequency of 399.72 MHz, a total of six fixed capacitors (5.1 pF, B-series; American Technical Ceramics and Dalian Dalicap Co., Ltd.) and one variable capacitor (2320-2; Johanson
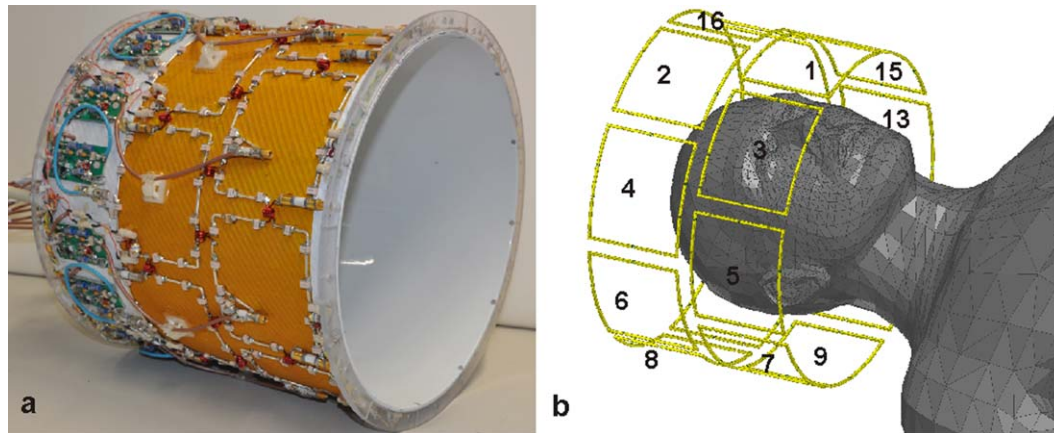
FIG. 1. **a:** Photograph of the transceiver array hardware with coil elements and the TR switches. **b:** Screenshot of the simulation model of the coil loaded with the phantom along with the assigned channel numbers. Only coil elements and human model are shown. [Color figure can be viewed in the online issue, which is available at wileyonlinelibrary.com.]

Manufacturing Corporation) were mounted in series. For the top-row elements, being smaller in size, five 6.2-pF fixed capacitors in combination with the variable capacitor were sufficient. Two capacitors in series were used at the input (Fig. 2b), one of which (matching capacitor [C_M]) was used for impedance matching whereas the other was part of the active detuning circuit, which also comprises a PIN diode (MA4P7470F-1072T; M/A-COM,

MA, USA) in series with a hand-wound inductor. The components of the input circuit consisting of matching, active detuning, and DC feed were assembled on a separate circuit board mounted on to the helmet. As secondary safety level, in case of malfunction of the detuning circuitry, a protection fuse (Siemens Healthcare) was incorporated on each channel. Solder pads made out of polyimide laminate were attached to the surface of the
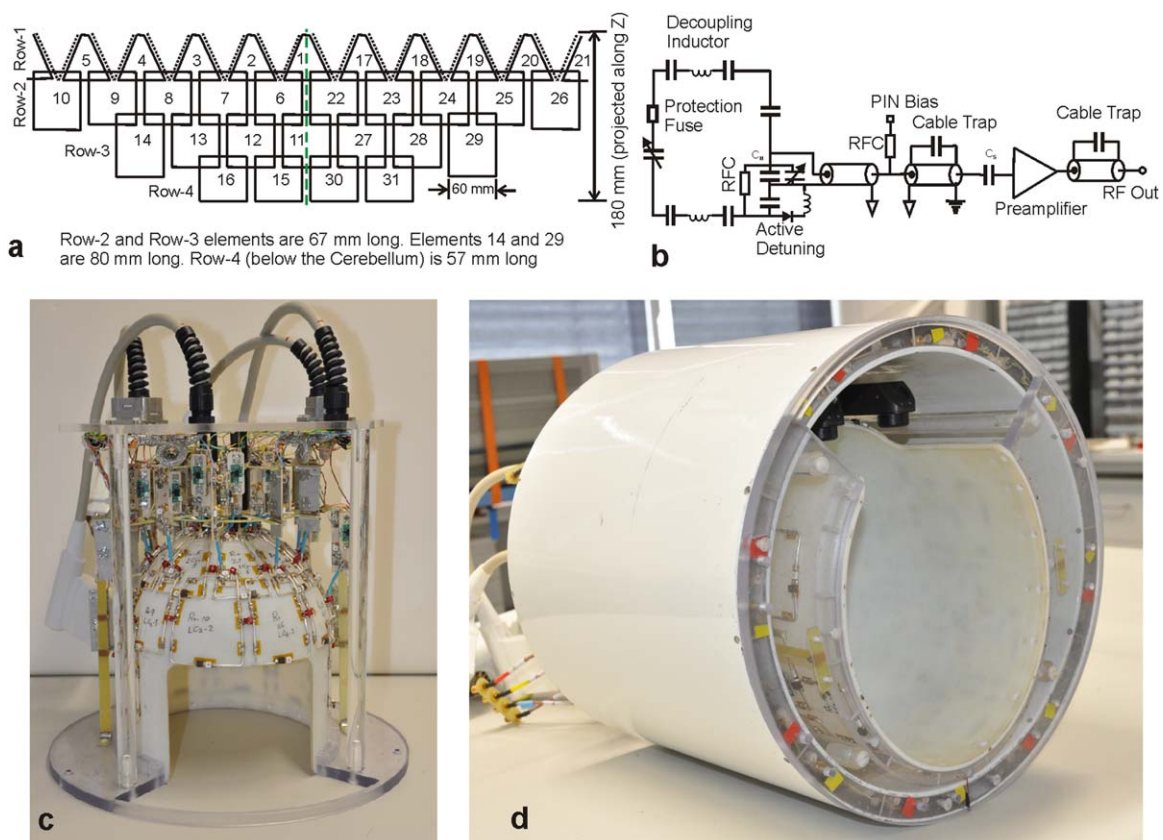

FIG. 2. Receive array. **a:** Two-dimensional view of the receive coil layout. Element dimensions are marked in the figure. **b:** Equivalent circuit schematic of a single element of the receive array. **c:** Photograph of the receive array. The socket on the top plate is used to plug-in the transmit array coil plugs. **d:** The final setup consists of the receive array and the periscopes assembled inside the transmit array. [Color figure can be viewed in the online issue, which is available at wileyonlinelibrary.com.]

helmet, and the components were soldered to these pads. Equal spacing between the capacitors was maintained. A 2-mm-diameter silver wire was used to connect these pads and to close the loop. A short coaxial cable connected the coil element with a circuit board, which consisted of two cable traps, one each at the input and output of the preamplifier, a series capacitor (C_S) to adjust the preamplifier decoupling (27), a bias tee and a low-noise preamplifier (WanTcom Inc., MN, USA). To protect the preamplifier from high voltage, a pair of PIN diodes (MPP4203; Microsemi, MN, USA) was added across the input of the high-electron mobility transistor (HEMT). The preamplifiers were assembled parallel to the B_0 field, and the circuit boards present inside the transmit field were oriented in such a way that its ground plane provides minimal shielding effect. The output cables are bunched together into four cable bundles, each with a cable trap across the outer sheath. Pictures of the receive array and the final setup are shown in Figures 2c and 2d, respectively. To allow for adding a fiber optics periscope for visual stimulation, the receive array was lowered in the AP direction (Fig. 2d).

Scanner Interface

The scanner has four coil sockets, each with eight bias lines that gives a total of 32 bias lines to control the two arrays. Eight bias lines were used to control 16 TR switches and another eight for active detuning of the 16 transmit elements. The remaining 16 bias lines were used to actively detune the receive array elements. To ensure equal splitting of the current to the shared elements, 43-Ω resistors were inserted in series with the bias lines in the input circuit board. The transmit array can be used in transceive mode (without the receive array) or in transmit-only receive-only (ToRo) mode. In transceive mode, the two coil plugs of the transmit array were connected directly to the scanner sockets. In ToRo mode, the four coil plugs of the receive array were plugged to the scanner sockets, and the DC signal to control the transmit array was routed from the receive array to two external sockets mounted on the top plate of the receive array (Fig. 2c), onto which the plugs of the transmit array were connected.

Coil Simulation

To accelerate the numerical analysis of the transmit array and to incorporate the effects of feeding/tuning/matching circuitry, a co-simulation approach consisting of an RF circuit simulator (ADS 2011.10; Agilent Technologies) and a 3D EM tool (HFSS 14; Ansys, PA, USA) was used for our investigation (28). The transmit array was tuned in the RF circuit domain, and then, the electric and magnetic field components were calculated together with SAR maps in the 3D EM domain. The realistic 3D EM model of the arrays included all coil construction details for the resonance elements, simulated with precise dimensions and electrical properties of the material. Series resistances (R_s) of 0.2 Ω for the PIN diodes and a Q of 200 at 400 MHz for the capacitors were assumed. Decoupling inductors and coil conductors were modeled with the same wire gauge as in the actual implementation. The head-gradient shield and the magnet bore were

included in the model. However, cable traps, RF cabling, and DC wiring were not included in the simulation. Only six components (feed-point, variable capacitor, and four decoupling ports) in each element were substituted by ports to reduce the time required for postprocessing and limit the amount of simulation data. Other distributed capacitors remained in the 3D EM domain. A multi-tissue human body model (29) extending up to the middle of the torso was scaled to mimic different head sizes (average head: $x = 0.9/y = 0.9/z = 0.9$; small head: 0.85/0.85/0.9; large head: 0.95/0.975/0.9). The position of the load was varied in the x–y plane to replicate the subject positions in the two different scanning modes: transceive mode, with the head position at the center, and the ToRo mode, in which the head was lowered to reproduce the head position inside the receive array. The locations and values of SAR_{10g} and the safe excitation efficiencies $\left(B_{1_{avg}}^+ / \sqrt{SAR_{10g}}\right)$ for the three body models were calculated for varying head positions along z-direction in 5-mm steps, where $B_{1_{avg}}^+$ is the value of B_1^+ averaged over the volume of interest. The investigation work flow in the numerical domain was as per the methods already presented (11,12). Because of the geometrical complexity of the receive array and some limitations in the 3D EM meshing, the receive array model was not incorporated in the numerical domain. Previous investigation of 7 T ToRo arrays (30) showed that a properly detuned receive array does not increase SAR_{10g}. Detuning of the receive array was validated by comparing field maps acquired with and without the actively detuned receive array in the transmit field. Uncertainty of SAR_{10g} due to the simplified numerical model was covered by an essential safety margin.

Transmit Field Characterization

The spatial distribution of the B_1^+ field generated by the transmit array was mapped in transceive mode and in ToRo mode. In transceive mode, the receive array was removed, and the receive signal was routed through the preamplifiers in the TR switches assembled in the transmit array. In the ToRo mode, the receive helmet was assembled inside the transmit array, and the signal was received using the 31 elements of the receive helmet. This comparison serves to establish the influence of the receive array hardware in the transmit field and to validate the performance of the active blocking networks in the receive array. An incremental transmit phase offset of ~22.5° between adjacent transmit elements was used to generate the CP mode. A presaturated turbo FLASH sequence (26) and the 3D actual flip angle imaging (AFI) technique (31) (field of view: $230 \times 201 \times 154$ mm³, matrix: $128 \times 56 \times 44$, TR_1/TR_2: 28/140 ms, echo time [TE]: 4.5 ms, bandwidth: 390 Hz/pixel, acquisition time: 10 min) were used for acquiring the field maps. The mean B_1^+ field produced by 1 V at the input of the matched coil was calculated for the measured transmit field and compared with the simulated field map.

Determination of the g-Factor

To determine the parallel imaging characteristics of the receive array, an average-sized head-and-shoulder phantom filled with tissue equivalent solution ($\varepsilon_r = 58.6$,

Table 1

S-parameters in dB showing the reflection and transmission parameters of the 16-channel transmit array when loaded with the head-and-shoulder phantom

Channel	1	2	3	4	5	6	7	8	9	10	11	12	13	14	15	16
1	−29	−14.8	−15.3	−23.3	−29.5	−28.3	−28.5	−28	−23.6	−32.6	−32.8	−23.4	−28	−34	−21.8	−18.5
2		−26	−14.5	−23	−21	−16	−19.2	−21.7	−44	−36.7	−31	−32	−26.5	−42	−17.9	−19.5
3			−21.5	−15.1	−16.3	−24	−25.8	−33.5	−33.5	−32.3	−25.8	−28.2	−48	−24	−34.5	−22.3
4				−24	−15.8	−18.8	−24.5	−18.8	−29.1	−27.8	−25.1	−32	−34.7	−32.5	−31.7	−30.3
5					−28	−15.9	−21.6	−25.9	−26.3	−30.7	−23.3	−29.7	−30.4	−25.2	−27.5	−19.5
6						−20	−13.7	−23.5	−30.3	−25.6	−32.7	−35	−30.4	−26.5	−26.5	−26
7							−27	−12.7	−18.8	−26	−28.3	−32.4	−39.2	−31.8	−27.7	−29.7
8								−25	−15.7	−14.4	−24.9	−27.8	−26.2	−29.5	−33.6	−39.3
9									−27	−13.7	−27	−24	−29.5	−35.5	−43	−25.1
10										−27	−14.1	−15.6	−27.9	−22.8	−21.2	−27.6
11											−26	−18.9	−18.8	−18.6	−18	−27.8
12												−35	−15.3	−14.1	−23.5	−24.6
13													−31	−15.5	−16.8	−16.6
14														−30	−12.8	−48
15															−36	−22
16																−28

$\sigma = 0.64$ S/m) (32) was scanned with a 3D gradient echo sequence (field of view: $256 \times 208 \times 160$ mm^3, voxel size: $1 \times 1 \times 1$ mm^3, TR = 8 ms, TE = 2 ms), using the GRAPPA parallel imaging technique with reduction factors (R) of 2, 3, and 4 in the AP direction. Each scan was repeated 15 times, and the mean values and standard deviations over these 15 scans were determined for every pixel. The *g*-factor for each pixel in the entire brain volume was determined by the following equation:

$$g = \frac{\text{SNR}_{R=1}}{\text{SNR}_R} \cdot \sqrt{\frac{T_R}{T_{R=1}}},$$ [1]

where SNR_R and $\text{SNR}_{R=1}$ are the SNRs in the accelerated and the nonaccelerated images, respectively, and T_R and $T_{R=1}$ are the corresponding scan durations.

SNR Comparison

To be able to assess the receive sensitivity of the presented array, a comparison to a previously published elliptical transceive array with 16 microstrip elements (4) was performed. For both coils, the head-and-shoulder phantom was used to obtain 3D gradient echo images with low flip angle and similar parameters as for the *g*-factor maps. In addition, the imaging experiment was repeated with a flip angle of zero to measure the noise distribution, and a flip angle map was generated using AFI (31). An SNR map over the entire volume was generated, and the flip angle map was used together with the known T_1 value of the phantom to calculate the SNR that would be reached with a flip angle of 90° and infinite repetition time (SNR_{90}) using the following equation:

$$\text{SNR}_{90} = \text{SNR} \cdot \frac{1 - \cos\alpha \cdot e^{-T_R/T_1}}{(1 - e^{-T_R/T_1}) \cdot \sin\alpha},$$ [2]

where α is the spatially varying flip angle as determined by the AFI measurement and T_R is the repetition time of the experiment.

RESULTS

Transmit Array

The head-and-shoulder phantom was used as the load for the bench measurements. Because of the lower loaded Q factor of the loop, the coil reflection and transmission parameters were less sensitive to load variations, and hence, the coil was not retuned to individual subjects. As the transmit array was shielded by the head gradient insert, the bench measurements were done by positioning the coil inside a bore simulator that mimics the influence of the head gradient. A self-built test-jig was used to provide the control signals to the coil as in the scanner. The coil reflection and transmission coefficients were measured through the TR switch, which was switched to transmit mode using the test-jig. The return loss on each transmit channel was adjusted to at least −20 dB in the loaded condition. To show the decoupling between all coil elements in transmit condition, the complete *S*-parameter matrix is tabulated in Table 1 with the element numbering from Figure 1b. All neighboring elements, both within the row and between the rows, and the non-neighboring elements were well decoupled. The quality of active detuning was measured using a pair of decoupled flux probes. The active detuning PIN diodes provided −30 dB of isolation when 50 mA current was supplied to each coil element. The TR switches with built-in preamplifiers provided a gain of 27 dB, a noise figure of 0.8 dB and 41 dB of protection from transmit RF. The noise correlation matrix that shows the coupling in the receive condition is shown in Figure 3a. In this plot, the average decoupling between all neighboring elements is −18 dB.

Receive Array

The unloaded Q (Q_{UL}) of a single receive element, measured in an unshielded environment and which also contained the decoupling inductor, was 190. Q_{UL} dropped to 160 when the protection fuse and active detuning circuit were added. The unloaded to loaded
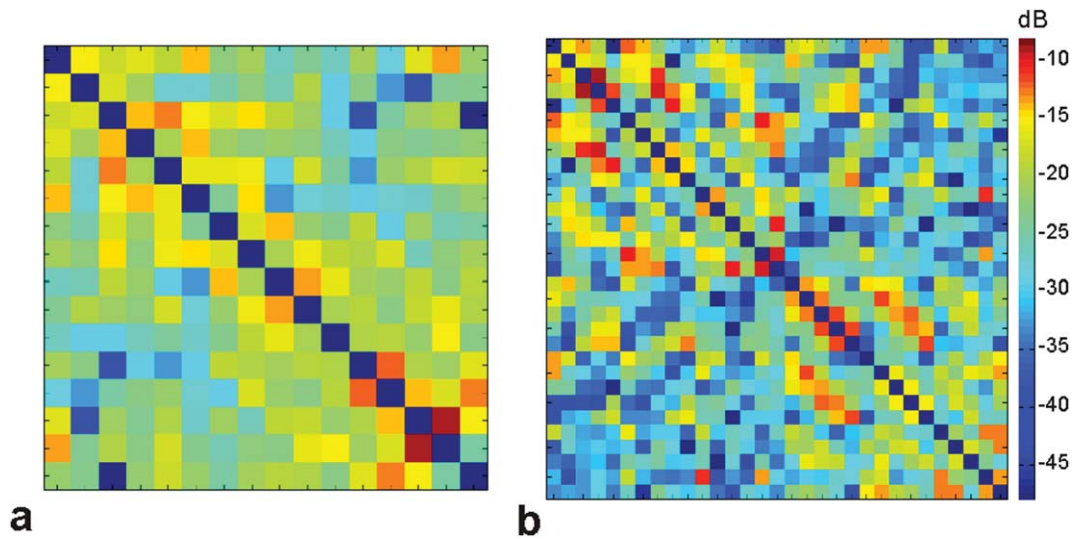
FIG. 3. Noise correlation plots in decibels. **a:** Transmit array: The average coupling between adjacent elements in the transceive mode is −18 dB. **b:** Receive array: Average value of the adjacent element decoupling is −15.6 dB, and the average of all off-diagonal values is −25.9 dB.

Q ratio (Q_{UL}/Q_L), depending on the proximity of the receive element to the load, varied between 8 and 12, indicating sample noise dominance. The average PIN diode detuning measured with a pair of decoupled flux probes was −36 dB with 50 mA of DC. The coil was loaded with the head-and-shoulder phantom, and the impedance matching and adjacent element decoupling were determined with all coil elements in tuned condition. The capacitors C_M and C_S influence both impedance match and preamplifier decoupling and hence were both adjusted iteratively. A target impedance match of −15 dB

was achieved on all the channels. Preamplifier decoupling was measured in an unloaded coil with two elements in tuned state (each PIN bias line controls two channels), whereas all other elements were actively detuned. The difference between the S_{21} values measured with a pair of decoupled flux probes, when the coil was terminated to 50 Ω and then to the low input impedance preamplifier, was −23 dB.

Figure 3b shows the noise correlation matrix of the receive array when loaded with the head-and-shoulder phantom. The plot shows that the coil element layout
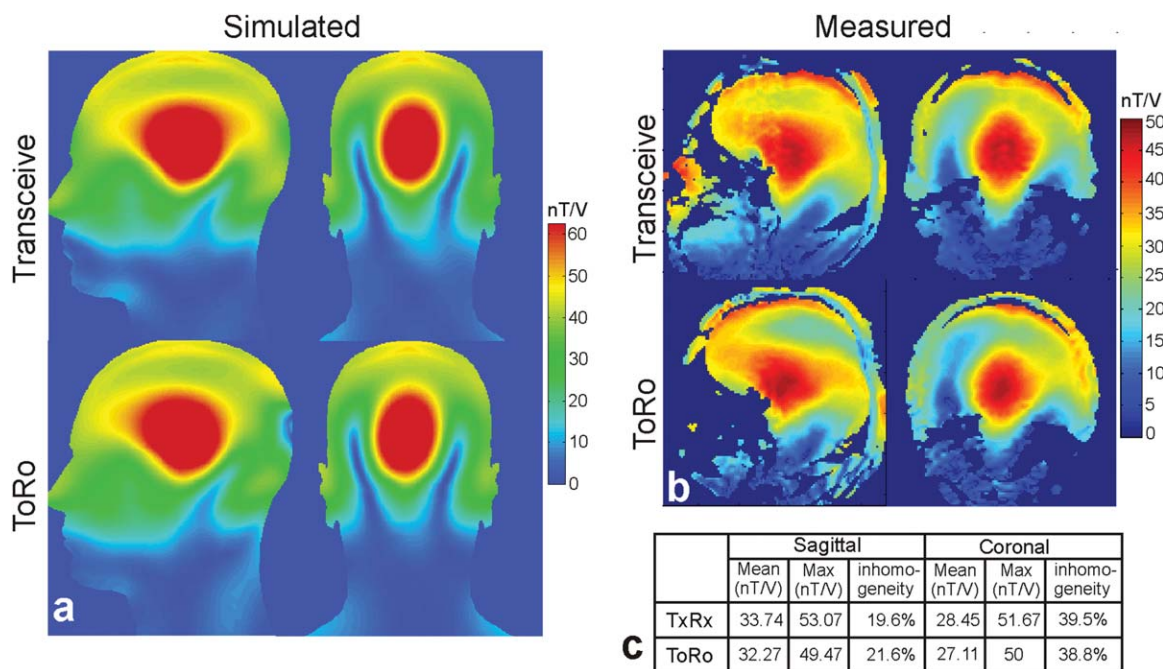

FIG. 4. Transmit field (B_1^+) maps in the two scan modes. The head is centered in the transmit array in transceive mode and offset in the AP direction in ToRo mode. **a:** Central sagittal and coronal slices of the simulated field maps. **b:** Measured field maps. **c:** A comparison of the measured field maps (in nT/V) in the two scan modes to estimate the influence of the receive array on the transmit performance.

	Sagittal			Coronal		
	Mean (nT/V)	Max (nT/V)	inhomo-geneity	Mean (nT/V)	Max (nT/V)	inhomo-geneity
TxRx	33.74	53.07	19.6%	28.45	51.67	39.5%
ToRo	32.27	49.47	21.6%	27.11	50	38.8%

used for constructing the receive array provides very good decoupling. The maximum value in this plot was −8.95 dB, and the average isolation achieved between all the adjacent element pairs was −15.6 dB. The average of all the off-diagonal values in the matrix was −25.9 dB.

Transmit Field Characterization and SAR

The first row in Figure 4a shows sagittal and coronal views of the simulated field maps in transceive mode, whereas the second row shows the corresponding field maps in ToRo mode. The variation in the transmit field distribution as seen in the central sagittal slice, particularly in the back of the head where the subject is closest to the transmit elements, is due to the lowered position of the load in the ToRo mode. For brain volume superior to the cerebellum, the CP mode provides a relatively efficient excitation. However, a characteristic arc due to field cancellation can be seen across the cerebellum, which is typical of CP mode excitation at 9.4 T. Hence, the uniformity and excitation efficiency were calculated for the brain volume superior to the cerebellum. To extend the excitation to the temporal lobe and to the cerebellum, RF shimming methods (33) are essential.

The measured field maps using the two scan modes are shown in Figure 4b. The transmit efficiency, measured on a $2 \times 2 \times 2$ cm^3 volume in the center of the brain, was 47.33 nT/V. In ToRo mode, the measured transmit field was altered in the back of the head. This is not due to the presence of the receive array but to the lowered head position as predicted in the simulated sagittal field map. Furthermore, field maps were acquired in the two scan modes with the same subject, maintaining the same position inside the transmit array, to determine the influence of the receive array on the transmit performance. Figure 4c shows statistics of the comparison from a region of interest drawn on the central sagittal and coronal slices covering the brain superior to the cerebellum. The drop in the mean transmit field in the presence of the receive array was less than 5%, indicating sufficient decoupling between transmit and receive arrays.

The mean transmit efficiency in CP mode, calculated from the measured field maps in the whole brain volume superior to the cerebellum, was 28.67 nT/V with an inhomogeneity of 24.9%. This means that a pulse length of 916 µs would be required to achieve a mean flip angle of 90° over the brain volume using a 1-kW hard pulse. The transmit efficiency of this array is lower than that reported earlier at 7 T (6,8) because of the much larger coil size, increase in coil and tissue losses at 9.4 T, and a different RF shim setting. The mean transmit efficiency from the simulated dataset was 40.8 nT/V for the corresponding volume. The additional losses in the measured transmit field are due to a number of factors such as differences in the load, solder joints, the complex cabling involved in the transmit array design, which were not included in the simulation and possible mismatches in the excitation phase.

An estimate of the power budget obtained from the numerical model is shown in Figure 5a. About 43% of the transmit power was delivered to the tissue. The most
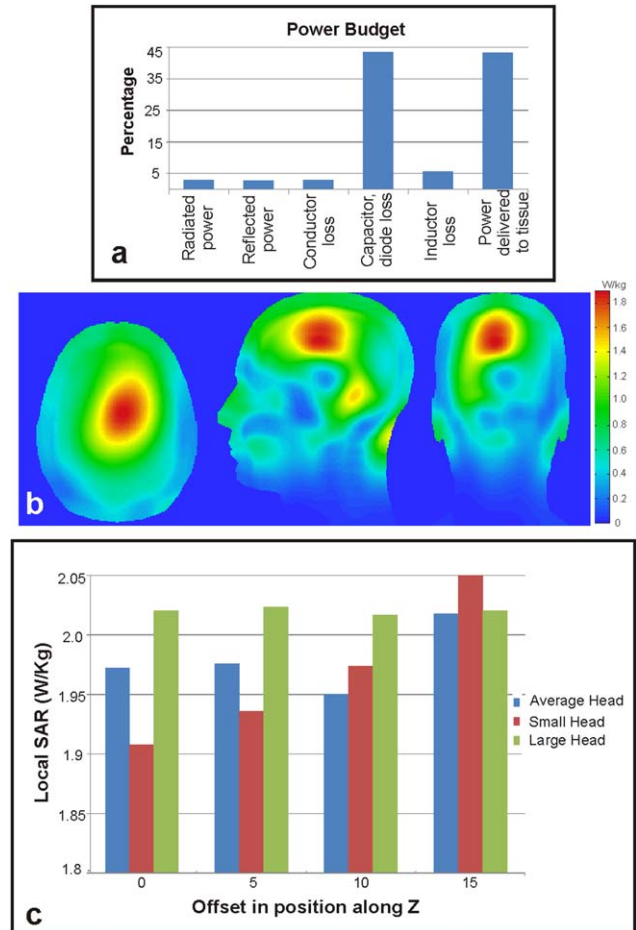

FIG. 5. **a:** Power budget analysis showing the distribution of the total input power. **b:** SAR_{10g} for the 2×8 transmit array in CP mode excitation. **c:** Dependence of local SAR_{10g} to different head size and position. A transmit power of 8 W was used in b and c. [Color figure can be viewed in the online issue, which is available at wileyonlinelibrary.com.]

significant loss factor is the capacitor loss that accounts for 44%. Losses to the coil components increase largely because of the increase in dielectric loss due to the lower Q of the capacitors. To measure the temperature rise on coil components, an RF source was connected to a single transmit element (all other elements terminated to 50 Ω) for 30 min and set to the maximum power as limited by the SAR settings. The maximum temperature rise, measured using a fiber optic probe, was 5.2°C on the diode and 3.6°C on the capacitors and well within the component specifications. Furthermore, no variation in S-parameter was observed before and after the heat test.

The calculated SAR_{10g} profiles are shown in Figure 5b. The peak SAR_{10g} was 1.8975 W/kg in the CP mode. To understand the robustness of the transmit array configuration, the dependence of peak SAR_{10g} on different head sizes and its positional variation is plotted in Figure 5c. To ensure safety in subject measurements, the transmit power was limited based on the maximum of the estimated local SAR_{10g}, adding a safety margin of 100%. This is in addition to the overestimation of SAR_{10g} due to the stronger B_1^+ in the numerical domain.

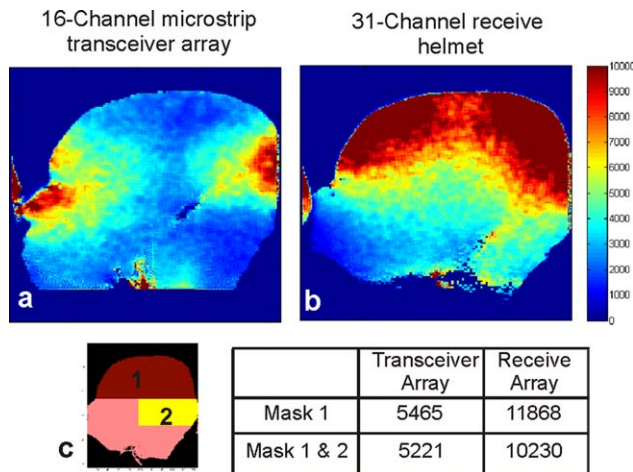FIG. 6. SNR comparison. **a:** SNR map of the 16-channel microstrip transceive array on the head-and-shoulder phantom. **b:** SNR map of the 31-channel receive array. Same color scale is used for both maps. **c:** Representation of the mask used for the SNR calculation and the SNR from the respective volumes. [Color figure can be viewed in the online issue, which is available at wileyonlinelibrary.com.]

Receive Array Performance

Figure 6 shows receive SNR maps of the head-and-shoulder phantom, extrapolated to a flip angle of 90° and long TR, for the presented coil in comparison with a 16-channel microstrip array (4). Two masks, one covering the brain volume superior to the cerebellum and the second mask covering the brain volume with the cerebellum, were created. The SNR gain in the first volume was a factor of 2.17, and in the entire volume represented by masks 1 and 2 was 1.96. This gain is due to the smaller size of the receive elements and their proximity to the head in the close-fitting helmet.

Figure 7 shows g-factor maps, acquired with the receive array loaded with the head-and-shoulder phantom, for acceleration up to a factor of 4 in the AP direction. The average g-factors (G_{avg1} and G_{avg12}) were calculated for the whole volume represented by the masks shown in Figure 6. The noise amplification remained sufficiently low, demonstrating good parallel imaging behavior. The g-factor values of less than 1 are
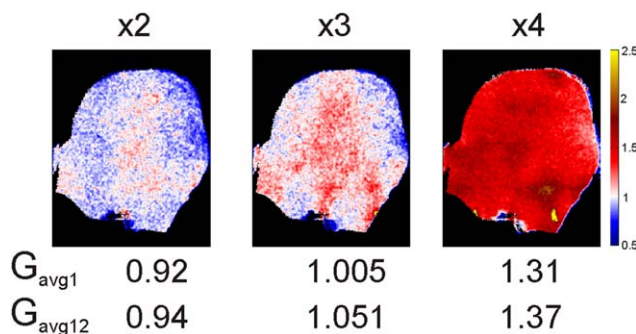
due to noise cancellation in the reconstruction process and are a well-known feature of GRAPPA (34,35). Figure 8 demonstrates the parallel imaging capability of the receive array with GRAPPA acceleration in two directions with no visible artifacts even up to an acceleration factor of 8.

Figure 9 shows high-resolution in vivo FLASH images without intensity correction acquired with the receive array. For these images, a slice-selective B_1 phase shimming approach (33) was used to optimize the transmit phase required for improved B_1^+ homogeneity. The calculated phase offsets for the individual channels were realized by inserting coaxial cables as phase shifters in the transmit path. The estimated phase depends on the cost function used in the shim algorithm (homogeneity/efficiency; Ref. 13), slice position and orientation, reflection and coupling characteristics of the coil, and size and shape of the head and its position inside the coil. These images demonstrate the ability to influence the B_1^+ field in all three spatial directions and to mitigate the severe B_1^+ artifacts typically present in the lower brain at 9.4 T.

DISCUSSION AND CONCLUSION

Currently, transceiver array coils are used in most applications that require multichannel transmit at UHF. In contrast, receive arrays are being used in almost every MRI examination at clinical field strengths because of their superior receive sensitivity. The close-fitting transceiver arrays reach high transmit efficiency; however, these arrays require time-consuming, subject-specific adjustments before each scan session. In this work, at 9.4 T, a receive array was successfully combined with a transmit array, which provides the capability to modulate the transmit field in all three directions. Time-consuming tune and match adjustments are not necessary, thus providing a simple and fast setup, comparable with clinical routine examination. The coil combination provides high receive sensitivity when compared with a transceiver approach, although at the cost of reduced
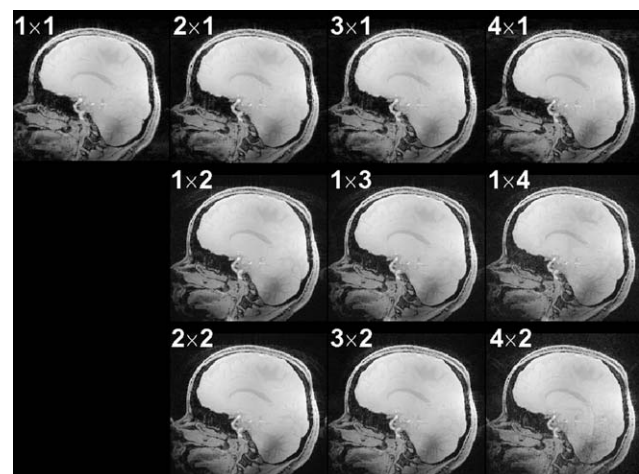

FIG. 7. The g-factor maps for the receive array with acceleration factor up to 4 in the AP direction. The mean g-factors for the volumes represented in Figure 6 are shown for each acceleration factor. [Color figure can be viewed in the online issue, which is available at wileyonlinelibrary.com.]

FIG. 8. Gradient echo images with GRAPPA acceleration in two directions: In the image, $i \times j$ corresponds to anterior–posterior × right–left (in-plane × through-plane).

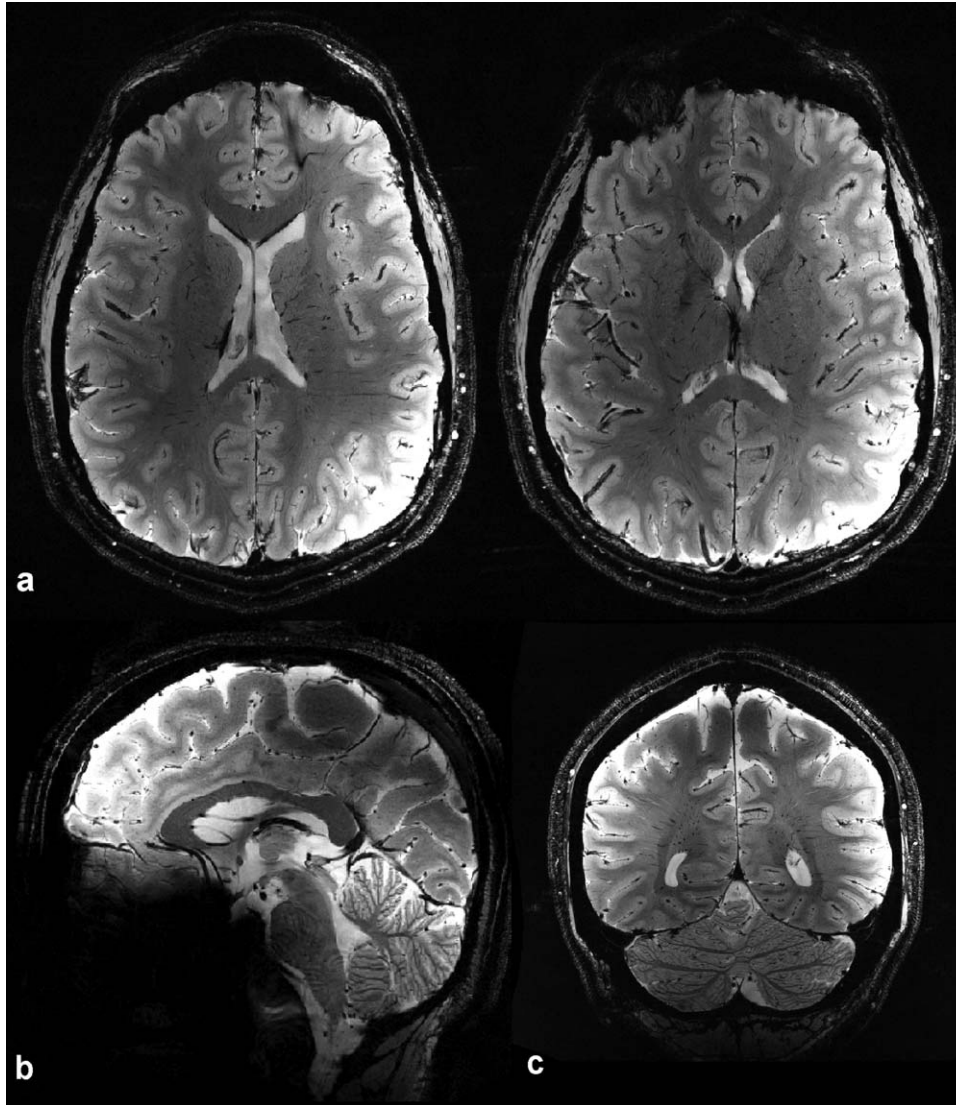FIG. 9. RF-shimmed in vivo images: (**a**) axial view: TE = 14 ms, TR = 400 ms, 260 μm in-plane resolution (702 × 832 matrix), slice thickness (ST) = 1 mm, nominal flip angle (FA) = 35°, acquisition time (TA) = 4 min, 41 s; (**b**) sagittal view: TE = 14 ms, TR = 500 ms, 330 μm in-plane resolution (522 × 576 matrix), ST = 1 mm, FA = 25°, TA = 3 min, 48 s; (**c**) coronal view: TE = 14 ms, TR = 400 ms, 250 μm in-plane resolution (768 × 820 matrix), ST = 1 mm, FA = 25°, TA = 5 min, 12 s.

transmit efficiency due to the large size of the transmit array. Using an elliptic cross section that conforms more closely to the head than the currently used circular shape could help to further improve the transmit efficiency. In addition, the issue of increased coil component loss at 400 MHz should be addressed, which is currently a dominant loss factor.

At frequencies as high as 400 MHz, the capacitance across overlapped loop strips of the receive element is a significant factor and this increases capacitive coupling. Wiggins et al. (16) demonstrated the benefits of using wires for coil loop conductors at 3 T. By adopting this approach for the receive array design, the decoupling between overlapped coil elements could be improved to −15 dB from −11 dB due to reduced capacitive coupling. The SNR map in Figure 6 shows that SNR gain was achieved over the entire brain volume. However, the SNR in the region of the cerebellum is not as high as in the cortex, demonstrating the need for coil elements closely following the contours of the anatomy. Further adaptation of the coil shape to the head will complicate the electromechanical design of our setup. It would

require a split-top housing design for the receive array and either a sliding or a split-top design for the transmit array to allow subject positioning in the coil.

As the RF power from a single amplifier was split up to excite each coil element, our experimental results were restricted to CP mode and static phase shimming (33). An even simpler static shim approach, applying global phase offset between the two rows, provided improved homogeneity in the upper brain at the cost of slightly reduced transmit efficiency (9,11,12) when compared with the CP mode. The availability of parallel transmit systems with independent amplitude and phase control adds another degree of freedom to improve spin excitation in terms of homogeneity, power efficiency, or SAR reduction. The transmit and receive array combination presented here is an enabling hardware for all these approaches.

REFERENCES

1. Van de Moortele PF, Akgun C, Adriany G, Moeller S, Ritter J, Collins CM, Smith MB, Vaughan JT, Ugurbil K. B1 destructive interferences

and spatial phase patterns at 7T with a head transceiver array coil. Magn Reson Med 2005;54:1503–1518.

2. Vaughan JT, Delabarre L, Snyder C, et al. 9.4T human MRI: preliminary results. Magn Reson Med 2006;56:1274–1282.

3. Adriany G, Van de Moortele PF, Wiesinger F, et al. Transmit and receive transmission line arrays for 7T parallel imaging. Magn Reson Med 2005;53:434–445.

4. Shajan G, Hoffmann J, Budde J, Adriany G, Ugurbil K, Pohmann R. Design and evaluation of an RF front-end for 9.4T human MRI. Magn Reson Med 2011;66:596–604.

5. Avdievich NI, Pan JW, Kuznetsov AM, Hetherington HP. Variable geometry elliptical transceiver phased array for imaging of the human brain at 7T. In Proceedings of the 17th Annual Meeting of ISMRM, Honolulu, Hawaii, USA, 2009. p 3002.

6. Avdievich NI, Pan JW, Hetherington HP. Improved longitudinal coverage for human brain at 7T: A 16 element transceiver array. In Proceedings of the 19th Annual Meeting of ISMRM, Montreal, Canada, 2011. p 328.

7. Gilbert KM, Curtis AT, Gati JS, Klassen LM, Menon RS. A radiofrequency coil to facilitate B1+ shimming and parallel imaging acceleration in three dimensions at 7T. NMR Biomed 2011;24:815–823.

8. Gilbert KM, Belliveau JG, Curtis AT, Gati JS, Klassen LM, Menon RS. A conformal transceive array for 7T neuroimaging. Magn Reson Med 2012;67:1487–1496.

9. Adriany G, Gözübüyük A, Auerbach EJ, Van de Moortele PF, Anderson P, Vaughan JT, Ugurbil K. A 32 channel transmit/receive transmission line head array for 3D RF shimming. In Proceedings of the 15th Annual Meeting of ISMRM, Berlin, Germany, 2007. p 166.

10. Adriany G, Ritter J, Vaughan JT, Ugurbil K, Van de Moortele PF. Experimental verification of enhanced B1 shim performance with a Z-encoding RF coil array at 7 tesla. In Proceedings of the 18th Annual Meeting of ISMRM, Stockholm, Sweden, 2010. p 3831.

11. Kozlov M, Turner R. Analysis of RF transmit performance for a 7T dual row multichannel MRI loop array. In Proceedings of the 33rd Annual International Conference of the IEEE EMBS, Boston, MA, USA, 2011. pp 547–553.

12. Kozlov M, Turner R. Analysis of RF transmit performance for a multi-row multi-channel MRI loop array at 300 and 400 MHz. In Proceedings of the Asia-Pacific Microwave Conference, Melbourne, Australia, 2011. pp 1190–1193.

13. Shajan G, Hoffmann J, Scheffler K, Pohmann R. A 16-element dual-row transmit coil array for 3D RF shimming at 9.4T. In Proceedings of the 20th Annual Meeting of ISMRM, Melbourne, Australia, 2012. p 308.

14. Robitaille PM, Berliner LJ. Ultra high field magnetic resonance imaging (biological magnetic resonance), Vol. 26. Berlin: Springer. 131 pp.

15. Wiggins GC, Triantafyllou C, Potthast A, Reykowski A, Nittka M, Wald LL. 32-Channel 3 tesla receive-only phased array head coil with soccer-ball element geometry. Magn Reson Med 2006;56:216–223.

16. Wiggins GC, Polimeni JR, Potthast A, Schmitt M, Alagappan V, Wald LL. 96-Channel receive-only head coil for 3 tesla: design optimization and evaluation. Magn Reson Med 2009;62:754–762.

17. Wiggins GC, Wiggins CJ, Potthast A, Alagappan V, Kraff O, Reykowski A, Wald LL. A 32 channel receive-only head coil and detunable transmit birdcage coil for 7 tesla brain imaging. In Proceedings of the 14th Annual meeting of ISMRM, Seattle, Washington, USA, 2006. p 415.

18. Ledden PJ, Mareyam A, Wang S, Van Gelderen P, Duyn J. 32 Channel receive-only SENSE array for brain imaging at 7T. In Proceedings of the 15th Annual Meeting of ISMRM, Berlin, Germany, 2007. p 242.

19. Wright SM, Wald LL. Theory and application of array coils in MR spectroscopy. NMR Biomed 1997;10:394–410.

20. Pruessmann KP, Weiger M, Scheidegger MB, Boesiger P. SENSE: sensitivity encoding for fast MRI. Magn Reson Med 1999;42:952–962.

21. Sodickson DK, Manning WJ. Simultaneous acquisition of spatial harmonics (SMASH): fast imaging with radio frequency coil arrays. Magn Reson Med 1997;38:591–603.

22. Griswold MA, Jakob PM, Heidemann RM, Nittka M, Jellus V, Wang J, Kiefer B, Hasse A. Generalized autocalibrating partially parallel acquisitions (GRAPPA). Magn Reson Med 2002;47:1202–1210.

23. Wiesinger F, Van de Moortele PF, Adriany G, Zanche ND, Ugurbil K, Pruessmann KP. Potential and feasibility of parallel MRI at high field. NMR Biomed 2006;19:368–378.

24. Kokubunji TN, Soka TT, Kashiwa YM, Akishima EY, Katakura K. RF probe for MRI. US Patent 5,489,847, 1994.

25. Caverly RH, Hiuller G. Establishing the minimum reverse bias for a p-i-n diode in a high-power switch. IEEE Trans Microwave Theory Tech 1990;38:1938–1943.

26. Chung S, Kim D, Breton E, Axel L. Rapid B1+ mapping using a pre-conditioning RF pulse with TurboFLASH readout. Magn Reson Med 2010;64:439–446.

27. Roemer PB, Edelstein WA, Hayes CE, Souza SP, Mueller OM. The NMR phased array. Magn Reson Med 1990;16:192–225.

28. Kozlov M, Turner R. Fast MRI coil analysis based on 3-D electromagnetic and RF circuit co-simulation. J Magn Reson 2009;200:147–152.

29. Vogel M, Kleihorst R. Large-scale simulations including a human body model for MRI. In Proceedings of the IEEE Microwave Conference, Honolulu, Hawaii, USA, 2007. pp 1345–1348.

30. Kozlov M, Turner R. Comprehensive numerical study of 7T transmit-only, receive-only array coils. In Proceedings of the 18th Annual Meeting of ISMRM, Stockholm, 2010. p 1447.

31. Yarnykh VL. Actual flip-angle imaging in the pulsed steady state: a method for rapid three-dimensional mapping of the transmitted radiofrequency field. Magn Reson Med 2007;57:192–200.

32. Beck BL, Jenkins KA, Rocca JR, Fitzsimmons JR. Tissue-equivalent phantoms for high frequencies. Concepts Magn Reson B 2004;20:30–33.

33. Hoffmann J, Budde J, Shajan G, Pohmann R. Slice-selective B1 phase shimming at 9.4 tesla. In Proceedings of the 18th Annual Meeting of ISMRM, Stockholm, Sweden, 2010. p 1470.

34. Robson PM, Grant AK, Madhuranthakam AJ, Lattanzi R, Sodickson DK, McKenzies CA. Comprehensive quantification of signal-to-noise ratio and g-factor for image-based and k-space-based parallel imaging reconstructions. Magn Reson Med 2008;60:895–907.

35. Polimeni JR, Wiggins GC, Wald LL. Characterization of artifacts and noise enhancement introduced by GRAPPA reconstructions. In Proceedings of the 16th Annual Meeting of ISMRM, Toronto, Canada, 2008. p 1286.